CrossMark

Molecular imaging of activated platelets via antibody-targeted ultra-small iron oxide nanoparticles displaying unique dual MRI contrast

Hang T. Ta [a, b, *], Zhen Li [c, **, 1], Christoph E. Hagemeyer [d, e, 1], Gary Cowin [f],
Shaohua Zhang [c], Jathushan Palasubramaniam [d], Karen Alt [d, e], Xiaowei Wang [d, g],
Karlheinz Peter [d, g, 2], Andrew K. Whittaker [a, b, 2]

[a] Australian Institute for Bioengineering and Nanotechnology, The University of Queensland, Brisbane, Australia
[b] ARC Centre of Excellence in Convergent Bio-Nano Science and Technology, Australia
[c] Center for Molecular Imaging and Nuclear Medicine, School for Radiological and Interdisciplinary Sciences (RAD-X), Soochow University, Collaborative
Innovation Center of Radiation Medicine of Jiangsu Higher Education Institutions, Suzhou 215123, China
[d] Atherothrombosis and Vascular Laboratory, Baker IDI Heart and Diabetes Institute, Melbourne, Australia
[e] Australian Centre for Blood Diseases, Monash University, Melbourne, Australia
[f] Centre for Advanced Imaging, The University of Queensland, Brisbane, Australia
[g] Department of Medicine, Monash University, Melbourne, Australia

ARTICLE INFO

ABSTRACT

Magnetic resonance imaging (MRI) is a powerful and indispensable tool in medical research, clinical diagnosis, and patient care due to its high spatial resolution and non-limited penetration depth. The simultaneous use of positive and negative MRI imaging that employs the same contrast agents will significantly improve detection accuracy. Here we report the development of functional multimodal iron oxide nanoparticles for targeted MRI of atherothrombosis using a combination of chemical and biological conjugation techniques. Monodisperse, water-soluble and biocompatible ultra-small magnetic dual contrast iron oxide nanoparticles (DCIONs) were generated using a high-temperature co-precipitation route and appeared to be efficient positive and negative dual contrast agents for magnetic resonance imaging. Using a unique chemo-enzymatic approach involving copper-free click chemistry and *Staphylococcus aureus* sortase A enzyme conjugation, DCIONs were functionalized with single-chain antibodies (scFv) directed against activated platelets for targeting purposes. The DCIONs were also labelled with fluorescent molecules to allow for optical imaging. The antigen binding activity of the scFv was retained and resulted in the successful targeting of contrast agents to thrombosis as demonstrated in a range of *in vitro* and *in vivo* experiments. T_1- and T_2-weighted MRI of thrombi was recorded and demonstrated the great potential of dual T_1/T_2 contrast iron oxide particles in imaging of cardiovascular disease.

© 2017 Elsevier Ltd. All rights reserved.

1. Introduction

Despite significant advances in diagnostic and therapeutic technologies, cardiovascular disease (CVD) remains the global leading cause of death, accounting for 17.3 million deaths per year, and is expected to grow to more than 23.6 million by 2030 [1]. This represents 30% of all global deaths and 80% of this occurs in low- and middle-income countries. CVD claims more lives than all forms of cancers combined [1]. Of all CVDs, stroke and coronary artery disease account for more than 70% of all deaths [2].

The most common form of CVD and also the leading cause of sudden death is atherosclerosis, a chronic progressive inflammatory disease of the arterial vessels. The process of atherosclerosis involves a complex interplay between various cells, particular leukocytes and platelets [3]. Unstable, vulnerable atherosclerotic plaques can rupture and cause thrombosis, resulting in myocardial infarction (MI) and stroke. Recent studies have confirmed that

(micro)thrombi containing activated platelets exist long before the presentation of sudden coronary death, indicating that vessel occlusion is often preceded by a variable period of localized coagulation and inflammation [4]. Currently, the prevention of MI and stroke is limited due to the lack of sensitive imaging methods. Those available usually involve invasive procedures such as coronary angiograms, which are potentially associated with complications, including death caused by MI or bleeding. Hence, there is a great need for new diagnostic strategies to determine whether the individual patient is at risk of MI or stroke, which then would allow for effective and early preventative treatment and improved clinical outcome.

Molecular imaging, the non-invasive visualization of fundamental (disease) biomarkers in living organisms, holds the promise to transform the diagnosis of CVD, profoundly impacting future clinical CVD care. Non-invasive detection of thrombosis employs various contrast agents that are equipped with moieties targeting the biological features associated with thrombosis formation such as fibrin, factor XIII, and activated platelets [5,6]. Compared to other modalities, molecular MRI has great potential for thrombus detection. Unlike positron emission tomography (PET) or computed tomography (CT) methods, MRI does not employ ionizing radiation; unlike ultrasound and optical methods, MRI provides deep tissue penetration; and it is more advantageous than PET, because MRI has much higher spatial resolution (sub-millimeter). The principle drawback of molecular MRI is the lower sensitivity of contrast agent detection compared to nuclear techniques and therefore the choice of a highly abundant target and the design of sensitive and specific molecular probes are critical. For molecular imaging of thrombosis, platelets are an ideal choice for targeting since they are the major component of thrombi [7].

To achieve high accuracy of disease diagnosis, attempts to combine complementary information obtained from different imaging techniques, including MRI, PET, CT and optical microscopy [8–11] have been made. However, differences in depth penetrations and spatial/time resolutions of various imaging devices can lead to difficulties and discrepancies when matching images, resulting in interpretation inaccuracies [8,9]. The development of dual imaging strategies that employ a single imaging technique and a single instrumental system such as MRI would provide significant advantages.

There are two widely used T_1 and T_2/T_2^* - weighted MRI contrast agents. Gadolinium (Gd) based agents enhance signal due to T_1 shortening at lower concentrations providing positive image contrast. At high concentrations, e.g. in the bolus following injection, Gd agents null the signal due to T_2/T_2^* shortening. Iron oxide nanoparticles generally provide negative image contrast due to T_2/T_2^* shortening. The T_1 effect or bright spot imaging is preferred since the location of the imaging agent is more readily distinguishable from potential artefacts produced by tissue interfaces, hemorrhage or signal cancellations at water-fat interfaces, which all produce negative contrast effects [12]. T_1-weighted imaging is particularly advantageous in imaging of vessel thrombosis, as a sufficient T_1 shortening effect allows generation of positive contrast between a thrombus (appearing bright in the image) and surrounding tissues and blood (dark). T_2-contrast agents, such as magnetic iron oxide nanoparticles, have shown limited toxicity and have been proven to be one of the most promising contrast agents for clinical use because iron is naturally found in the body [13]. These agents can be detected at a relative lower concentration and a sub-millimeter areas using T_2-weighted or T_2^* (susceptibility) weighted imaging. However, the limitations of iron oxide agents include the lack of specificity in heterogeneous anatomy and potential confusion with effects from bleeding, calcification, metal deposits (such as endogenous iron) and other susceptibility artefacts [14].

Previously, several attempts have been reported on the development of MRI imaging agents for molecular imaging of atherosclerosis and thrombosis. Among these, Gd-based agents were widely employed to image endothelial dysfunction and activation [15]; extracellular matrix (ECM - the major component of atherosclerotic lesions) via targeting ECM proteins such as collagen [16], neovascularization by targeting the $\alpha v \beta 3$ integrin [17]: proteolytic enzymes during plaque development [18]; thrombus and plaque by targeting fibrin [19–24]; and lipids — the major components of atherosclerotic plaques [25,26]. Iron oxide nanoparticles were also used extensively to image endothelial dysfunction by targeting the expressed adhesion molecules on the endothelial surface [27]; macrophages resident in the plaques [28,29]; and thrombus via targeting GPIIb/IIIa receptors expressed on activated platelets [30–32]. Although research on molecular imaging of CVD has been reported extensively, these MR imaging agents used only single imaging modes such as T_1- or T_2/T_2^*-weighted imaging.

Since both T_1-positive and T_2-negative contrast agents have their respective advantages and disadvantages, it is highly desirable to prepare a robust dual contrast agent for overcoming the limitations of single modality contrast agents. The simultaneous use of a contrast agent that can provide both T_1 and T_2 effects will significantly improve detection accuracy. Previously, we have reported the synthesis of ultra-small, water-soluble and biocompatible magnetic iron oxide nanoparticles as positive and negative dual contrast agents [13]. Here we report the development and functionalization of these nanoparticles for targeted imaging of thrombosis. The nanoparticles were also labelled with near infrared dyes to enable optical detection, and functionalized with single-chain antibodies (scFv) for targeting to activated platelets, which are critical players in atherosclerosis, thrombosis, and inflammation [33,34]. Our strategic approach employing a dual mode, where two different T_1 and T_2-weighted imaging are performed simultaneously, can potentially provide highly sensitive and accurate diagnostic information.

2. Materials and methods

All reagents and solvents were obtained from standard commercial sources and were used as received.

2.1. Generation and production of proteins

ScFv$_{antiGPIIb/IIIa}$ and the control, non-binding antibody scFv$_{mut}$ was generated and produced as described previously [35–40]. The generation and production of the plasmid construct *Staphylococcus aureus* Sortase enzyme were described previously [37].

2.2. Synthesis of dual contrast iron oxide nanoparticles (DCIONs)

The synthesis of DCIONs has been described previously [13].

2.3. Characterization of DCIONs

Hydrodynamic size and zeta potential of nanoparticles were determined with a Zetasizer (Malvern). Thermal Gravimetric Analysis (TGA) was performed by heating sample at a heating rate of 10 °C/min from 30 to 100 °C, maintaining 100 °C for 30 min, then heating to 690 °C at a heating rate of 10 °C/min using Tolendo TGA/DSC-1 (Mettler).

2.4. Preparation of scFv-DCION constructs

The overall conjugation procedures to generate scFv-DCIONs are

summarized in Scheme 1.

2.4.1. Sortase reaction - conjugation of scFv-LPETG to GGG-N3 and purification of the coupled products

Using the bacterial transpeptidase Sortase A from *Staphylococcus aureus*, scFvs with C-terminal LPETGG tag were ligated to glycine containing substrate. Peptide NH_2-Glycine-CONH-PEG$_3$-N$_3$ (Purar Chemicals, Melbourne, Australia) were mixed with the scFv and Sortase A in a molar ratio of 3:1:3 in sortase reaction buffer (50 mM Tris, 150 mM NaCl, 0.5 mM CaCl$_2$ pH 8.0) for 5 h at 37 °C. The His-tag on the scFv was removed during this reaction. Purification using FPLC was used to remove the Sortase A enzyme, excess scFv with His-tag and the released His-tag containing C-terminal part of the scFv. The reaction mixture was applied to an anti-His tag Ni column. The flow-through containing the product was collected and dialyzed against PBS overnight at 4 °C. The efficiency of the coupling procedure was analyzed by SDS-PAGE and protein assay (BCA). The typical yield for this reaction is up to 90% as reported previously [39].

### 2.4.2. Conjugation of Cy7.5-NH$_2$ and scFv-N$_3$ to DCIONs

8 mg of DCIONs was dissolved in 50 μL of PBS pH7.2 and then 190 μL of dimethyl sulfoxide (DMSO, Sigma Aldrich) was added. The mixture was sonicated for 10 min and 200 μL of DMSO containing 8 mg 1-Ethyl-3-(3-dimethylamino-propyl)carbodiimide hydrochloride (EDC, Thermo Scientific) and 20 mg N-hydroxysuccinimide (NHS, Thermo Scientific) was added. After 5 min of sonication and 15 min of incubation at room temperature with shaking or rotating,

48 μL of 40 mM Cy7.5-amine (Lumiprobe) and 4.8 μL of 40 mM DBCO-PEG$_4$-amine (Click Chemistry Tools) were added, the mixture was sonicated for 5 min and the reaction was allowed to proceed at room temperature with shaking. After 16 h of incubation, 12 mL of phosphate buffer containing 0.05% Tween, pH 8.7 was added and the reaction mixture was filter-centrifuged using Amicon Ultra centrifugal filter unit (Amicon® Ultra-4 PLTK Ultracel-PL membrane, 30 kDa, Sigma Aldrich) according to manufacturer instruction. The DCIONs were then redispersed in the same buffer and let stand for 2 h to promote the hydrolysis of non-reacted NHS ester. All remaining non-reacted DBCO-PEG$_4$-amine, Cy7.5-amine, EDC and NHS were removed simultaneously with buffer exchange to either MES pH 6.0 or PBS pH 7.4 using Protein Desalting Column (Pierce). To attach the scFv onto the DCIONs, scFv-azide was added to the collected DCION solution at a ratio of 1:1 (DCION:scFv) unless specified differently. The reaction mixture was incubated for 3 h with shaking at 37 °C unless stated otherwise and the resultant scFv-DCIONs were store at 4 °C.

The conjugation efficacy and efficiency was evaluated via Fourier transform infrared spectroscopy, SDS-PAGE and agarose gel electrophoresis.

2.5. Flow cytometry

Flow cytometry was used to evaluate the binding capacity of scFv-N$_3$ to either platelets or Chinese Hamster Ovarian (CHO) cells expressing GPIIb/IIIa receptors. To test with platelets, blood from healthy volunteers was collected by venipuncture and centrifuged
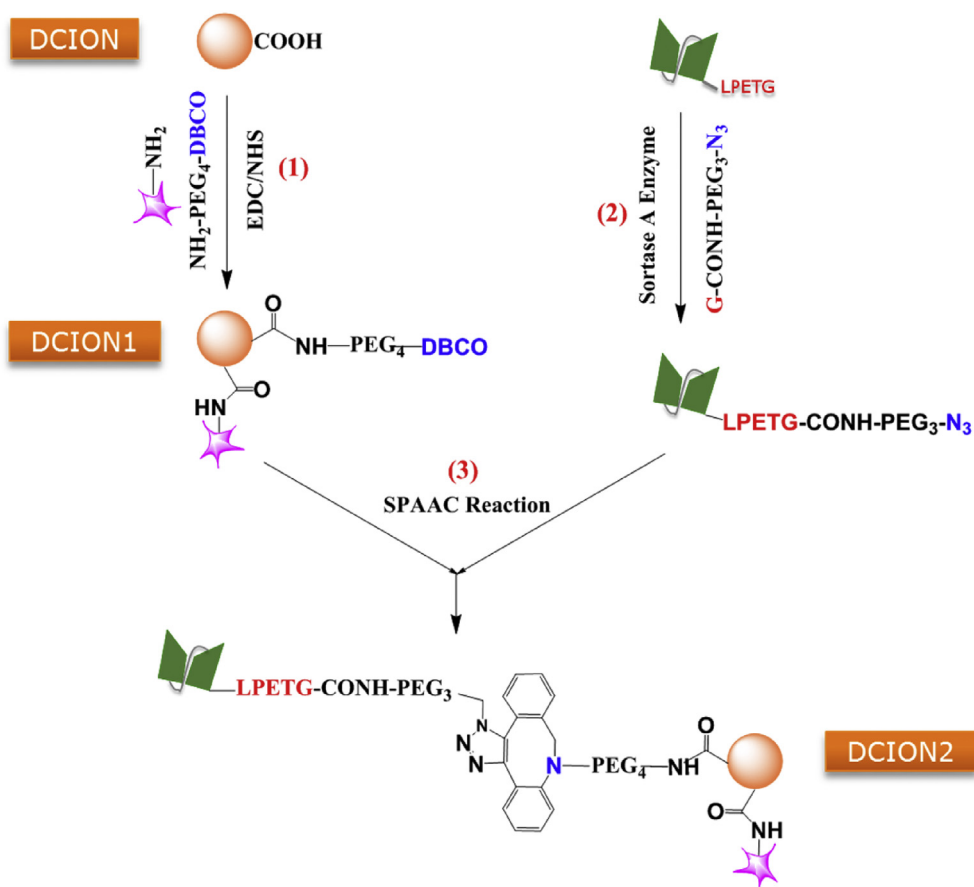
Scheme 1. Image illustrating the coupling procedures of DCIONs with NIR dyes and scFv. The protocol including (1) the introduction of the dyes and DBCO functional groups to the DCION surface via the carbodiimide reaction, carboxyl activation using EDC and NHS; (2) a sortase-mediated condensation reaction between scFv-LPETG and G-CONH-PEG$_3$-N$_3$ to attach azide functional groups to the scFv's C-terminus; (3) copper-free click conjugation between DBCO groups on DCIONs and N$_3$ groups on scFv molecules.

at 180 × g for 10 min to obtain Platelet Rich Plasma (PRP). Diluted platelet-rich plasma was either activated by 20 μM adenosine diphosphate (ADP, Sigma) or non-activated and incubated with scFv-N_3 constructs at room temperature. To test with CHO cells, 1×10^5 cells in 50 μL PBS (Ca, Mg) were incubated with scFv-N_3 at room temperature. After 10 min, the samples were incubated with 1 μL anti-V5 tag antibody (FITC) (1:10 dilution) (Abcam, ab1274), which selectively binds to the V5-tag on scFv molecules. Samples were then fixed and analyzed on either a FACS Aria Cell Sorter or Accuri C6 CFlow flow cytometer (BD Bioscience). Fluorescence signal was examined on 10,000 gated events.

2.6. Static adhesion immunofluorescence assay

CHO cells expressing the activated and non-activated GPIIb/IIIa receptors were used in this assay. Cells within 10 passages were seeded in a 96-well plate at a density of 30,000 cells per well in 100 μL of supplemented DMEM medium and incubated at 37 °C in a 5% CO_2 incubator for 5 h, after which scFv-DCIONs were added into the wells at different concentrations from 13 to 200 μg/mL scFv-DCIONs. The cells were incubated for 30 min at room temperature, washed 3 times with PBS, and then fixed with 2% paraformaldehyde (PFA). The fluorescence of the wells was imaged with a Carestream FX-Pro (Bruker Corporation). Cy7.5 images were collected with a spectral protocol utilizing excitation filter at 760 nm with collection through an 830 nm emission filter set (f-stop 2.80, 2 × 2 binning, 120 mm FOV, 10s exposure time). To provide location of the well, fluorescence images were co-registered with an X-ray image (f-stop 2.80, 0.2 mm aluminium filter, 120 mm FOV, 10s exposure time). All images were batch exported as 16-bit TIFF images and image processing was completed by Image-J (National Institute of Health, USA).

2.7. In vitro human thrombus adhesion assay and magnetic resonance imaging

Blood from healthy volunteers taking no medication was anti-coagulated with citric acid and centrifuged at 1000 rpm for 10 min. Of the resulting platelet rich plasma, 100 μL was incubated with 8.8 μL Actin (Dade Behring) and 2.5 μL of 1 M $CaCl_2$ to induce coagulation. Samples were incubated for 12 min at 37 °C in a water bath. The developed clots were stored for another 30 min at ambient temperature under continuous rotation. The clots were incubated with scFv-DCIONs for 15 min at room temperature with rotating and then extensively washed with PBS, fixed with 2% PFA and transferred into a 48-well plate. Cy7.5 images of the clots were collected using a Carestream FX-Pro (Bruker Corporation) with a spectral protocol utilizing excitation filter at 760 nm with collection through an 830 nm emission filter set (f-stop 2.80, 2 × 2 binning, 120 mm FOV, 5s exposure time). To provide location of the clots, fluorescence images were co-registered with a reflectance image (f-stop 2.80, reflectance filter, 120 mm FOV, 0.2s exposure time). All images were batch exported as 16-bit TIFF images and image processing was completed by Image-J (National Institute of Health, USA).

After fluorescence imaging, the clots were embedded into 2% low melting point agarose (Sigma). Magnetic resonance imaging (MRI) of agarose-embedded clots was performed on a 9.4 T scanner (Bruker). The embedded clots were placed within a MRI coil, having the longitudinal axes of the cone-shaped clots oriented horizontally. The parameters used for T1-weighted imaging were: echo time (TE) = 14 ms; repetition time (TR) = 1000 ms; matrix size = 256 × 256; field of view (FOV) = 4.0 × 4.0 cm^2 and slice thickness = 1 mm. The T2-weighted imaging was performed using MSME method under the same conditions except of longer TE (60 ms) and TR (2000 ms).

2.8. In vivo MR imaging

In vivo MRI experiments were conducted at the University of Queensland (Brisbane, Australia). Care and use of laboratory animals followed the national guidelines and were approved by the institutional animal care and ethics committees of the University of Queensland. 11-week old C57BL/6 wild-type mice (Animal Resources Centre, ARC, Western Australia) weighing 25 g were anaesthetized by intraperitoneal injection of a ketamine:xylazine mixture (100:20 mg/kg body weight). A catheter was placed into tail vein to facilitate injection. Carotid arterial wall-adherent thrombosis was induced with 12% aluminium chloride. A small filter paper (2 mm × 1 mm) saturated with 12% $AlCl_3$ was placed under the left carotid artery of the animal for 3 min. Animals were transferred into a preclinical MRI system, comprising a 300 mm bore 7 T ClinScan, running Siemens VB17. A 23 mm ID mouse head MRI rf coil was used to acquire the images. The animal was connected to an ECG and breathing rate monitor and placed in the animal bed. Vital signs were monitored throughout the entire experiment. Anaesthesia was gradually switched from ketamine/xylazine to 0.5−1% isoflurane in oxygen and maintained a breathing rate of 40−60 breaths per minute. Three orthogonal gradient echo images (localiser images) were acquired with the following parameters: TR = 23 ms, TE = 4.43 ms, field of view 40 × 40 mm, slice thickness = 1 mm, matrix = 256 × 256, flip angle = 25°, bandwidth = 260 Hz/Px. A 3D transverse vibe image (3D flow enhanced image) was acquired to highlight flow in the arteries using the following parameters: TR = 30 ms, TE = 1.72 ms, field of view = 25 × 25 × 16 mm, matrix = 384 × 384 X 80, resolution = 65 × 65 × 200 μm, flip angle = 21°, bandwidth = 520 Hz/Px. 2D T1 weighted spin echo images (2D spin echo image) were acquired using the following parameters: TR = 430 ms, TE = 12 ms, field of view 20 × 20, slice thickness = 0.4 mm, image matrix = 192 × 192, resolution = 104 × 104 μm, flip angle = 90°, bandwidth = 130 Hz/Px, fat saturation, two 15 mm transverse saturation bands at the start and end of the slice package. 2D T2 weighted spin echo images (2D spin echo image) were acquired using the following parameters: TR = 2500, TE = 40 ms, field of view 20 × 20, slice thickness = 0.4 mm, image matrix = 192 × 192, resolution = 104 × 104 μm, flip angle = 90°, bandwidth = 130 Hz/Px, fat saturation, two 15 mm transverse saturation bands at the start and end of the slice package and one 5 mm saturation band anterior to the carotid artery and one 10 mm saturation band posterior to the carotid artery. After baseline scans, dual contrast iron oxide nanoparticles (0.32 mg Fe per kg mouse) were injected into mice via tail veins and the mice were scanned for T_1- and T_2-images at different time points. Region of interest (ROI) was manually placed over the artery and the ROI signal intensity was measured using OsiriX Lite. The effect of the contrast agent was evaluated by comparing the ratios of total change in signal within ROI in post-agent images (S_n) and those in baseline images (S_0).

2.9. Histological analysis

After in vivo MRI was performed, animals were deeply anaesthetized with ketamine and xylazine. The injured carotid artery was removed, washed in PBS and fixed with 4% PFA. The artery was washed 3 times with PBS and then added into 15% sucrose in 1XPBS at 4 °C until it sunk. The artery was then transferred into 30% sucrose in 1XPBS at 4 °C. Once it sunk, it was blot dried and placed in Optical Coherence Tomography (OCT) TissueTek (Sakura Finetec) at 4 °C. Sample was then frozen using dry ice and cut into 10 μm thick

cross-sections on a cryostat (Thermo Fisher Scientific). Tissue sections were allowed to dry at room temperature and Masson's trichrome staining of the tissue was performed. Histology images were taken using an inverted microscope (IX51, Olympus) with digital colour camera (Olympus) and QCapture Pro6.0 software (QImaging).

2.10. Statistical analysis

Results are presented as mean $\pm$ standard error of the mean (SEM). Data were analyzed for statistical significance using two-way ANOVA analysis with Bonferroni's multiple-comparison post-test (GraphPad Prism 7). A probability value (P) $\leq$ 0.05 was considered significant.

3. Results and discussion

The present work is the first report on imaging of cardiovascular disease or thrombosis using MRI dual positive and negative 3.3 nm iron oxide contrast agents (DCIONs). The scFv-tagged DCIONs were prepared using a unique chemo-enzymatic approach involving copper-free click chemistry and *Staphylococcus aureus* sortase A enzyme conjugation. The antigen binding activity of the scFv-DCIONs was evaluated in a range of *in vitro* and *in vivo* experiments, including binding to *in vitro* human thrombi and *in vivo* mouse carotid thrombosis. T_1- and T_2-weighted MRI of both *in vitro* human thrombus and *in vivo* mouse carotid arterial thrombosis were performed with the objective to enable self-confirmation of images and leads to a greater diagnostic accuracy.

3.1. Synthesis and characterization of DCIONs

Using a high-temperature co-precipitation method developed by Li et al. [13], monodispersed ultra-small water-soluble DCIONs have been synthesized without post surface modification. Tri-thiol terminated poly (methacrylic acid) (PMAA-PTTM, M_n = 6360 g/mol, M_w = 7520 g/mol) was used as a stabilizer to effectively prevent aggregation of nanoparticles and to ensure a small particle size

[13]. The polymer also provides reactive carboxylic groups on the surface of DCIONs for introducing other functionalities. These nanoparticles have excellent water-solubility with a hydrodynamic size of 7.7 nm and a zeta potential of −40 mV as determined by dynamic light scattering (DLS − Table S1). Thermal gravimetric analysis (TGA) of the DCIONs was performed and the results are shown in Fig. S1. Two decomposition stages or two derivative peaks were observed in the TGA curve. The first peak with a percentage mass loss of 12% was at 225 °C and is due to the decomposition of terminal thiol groups from the polymer PMAA-PTTM. The weight loss of 25% measured for the second peak at 422 °C represents the loss of the side group and the polymer backbone. From these TGA data, the weight percentage of polymer coating on the surface of DCION was approximately 37%.

MRI images of DCIONs at different concentrations were collected using a 9.4 T MRI scanner at room temperature (Fig. 1). Here DCIONs show their capacity to not only enhance the signal in T_1-weighted imaging (shorten T_1 relaxation time) but also decrease the signal in T_2-weighted imaging (shorten T_2 relaxation time). Both T_1- and T_2-weighted images demonstrate the strong dependence of signal intensity on iron concentration with longitudinal relaxivity (r_1) and transversal relaxivity (r_2) measured as 5.3 and 73.4 mM^{-1}s^{-1}, respectively. DCIONs appear to have pronounced longitudinal relaxivities and a relatively small r_2/r_1 ratio ($r_2/r_1 = 13$) compared to other iron-based contrast agents at preclinical high field strength (9.4 T) such as ultra-small superparamagnetic iron oxide nanoparticle SHU-555C ($r_2/r_1 = 256$) [41], suggesting their potential as dual positive and negative contrast agents.

A number of studies have been reported for the synthesis of such dual mode MRI contrast agents. Ultra-small superparamagnetic iron oxide (USPIO), which displays both T_1 and T_2 contrast effects have been developed as summarized in Table S2 [42–48]. Xue et al. have reported the use of 3.5 nm iron oxide nanoparticles for dual-modality MRI of tumor angiogenesis, recently [49]. In general, both T_1 and T_2 (or T_2^*) relaxation times are shortened by iron oxide particles, however, the magnetic susceptibility effect of superparamagnetic iron oxide nanoparticles is generally dominant over longitudinal relaxation to give a much
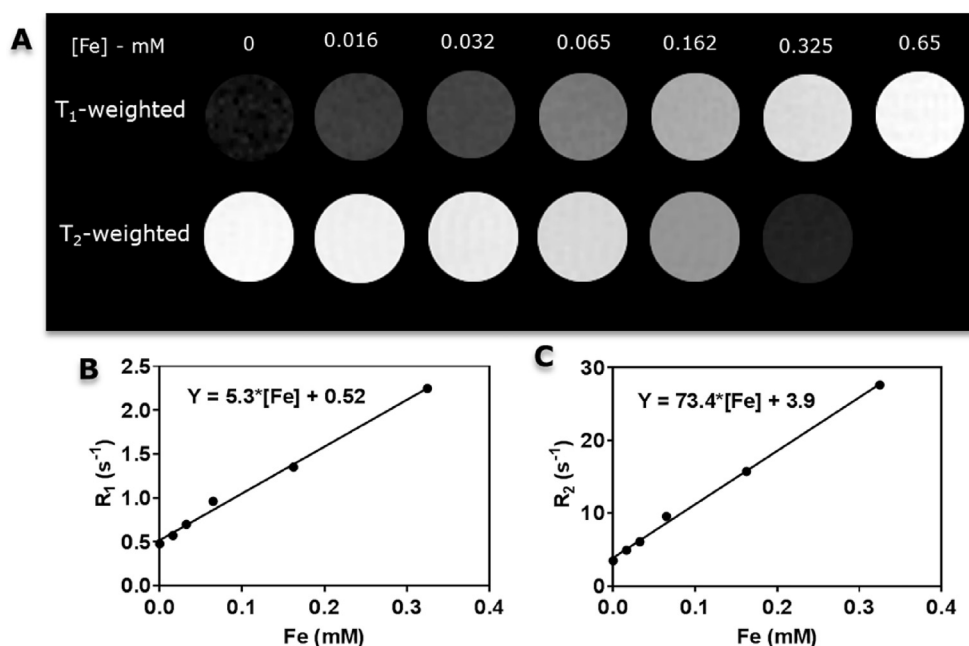

Fig. 1. *In vitro* T_1- and T_2-weighted images (**A**) and relaxivities (**B**) of DCIONs recorded on a 9.4 T scanner.

greater r_2/r_1 ratio (r_1 and r_2 are longitudinal and transverse relaxivities, respectively) than paramagnetic molecules such as Gd-DTPA [50]. Particularly, signal dephasing from reduced T_2 or T_2^* is greater than signal enhancement due to the shorter T_1. USPIOs with sizes smaller than 6 nm are able of generating T_1-enhanced images owing to low magnetization by a strong surface spin-canting effect [42,43,47]. They showed good longitudinal and transverse relaxivities r_1 and r_2 with low r_2/r_1 ratios at low magnetic field strength (1.5 T). However, state-of-the art clinical MRI devices use magnets of greater strength at 3.0 T and 7.0 T, which raises questions about the feasibility and practicality of these USPIOs in modern clinical settings. Only one study reported USPIO relaxivities at 3 T [43], however, their r_1 and r_2 values were significantly lower than those from our dual contrast iron oxide nanoparticles (DCIONs).

Our DCIONs showed good T_1 and T_2 contrast effects compared with clinically positive contrast agent such as Gd-DTPA (Magnevist) and conventional negative contrast agent such as iron oxide SHU-555C (Resovist). At the near-clinical magnetic field strength of 4.7 T, the DCION longitudinal relaxivity ($r_1 = 8.3$ mM^{-1}s^{-1}) was larger than that of Gd-DTPA ($r_1 = 4.8$ mM^{-1}s^{-1}) and three times that of SHU-555C ($r_1 = 2.9$ mM^{-1}s^{-1}). The transversal relaxivity ($r_2 = 35.1$ mM^{-1}s^{-1}) of DCION was six times that of Gd-DTPA ($r_2 = 5.3$ mM^{-1}s^{-1}), and half that of SHU-555C ($r_2 = 69$ mM^{-1}s^{-1}) [13]. At 4.7 T, the ratio r_2/r_1 of DCION was 4.2 while that of Gd-DTPA was 1.1 and that of SHU-555C was 23.8.

At the preclinical field strength of 9.4 T, r_1 of SHU-555C was much lower than r_2 ($r_1 = 1$, $r_2 = 256$ mM^{-1}s^{-1}, $r_2/r_1 = 265$) [41] while both r_1 and r_2 of Gd-DTPA appeared smaller ($r_1 = 3.9$, $r_2 = 4.2$ mM^{-1}s^{-1}, $r_2/r_1 = 1.1$) [51]. At 9.4 T, our DCION showed a decrease in r_1 and an increase in $50r_2$ ($r_1 = 5.3$, $r_2 = 73.4$ mM^{-1}s^{-1},
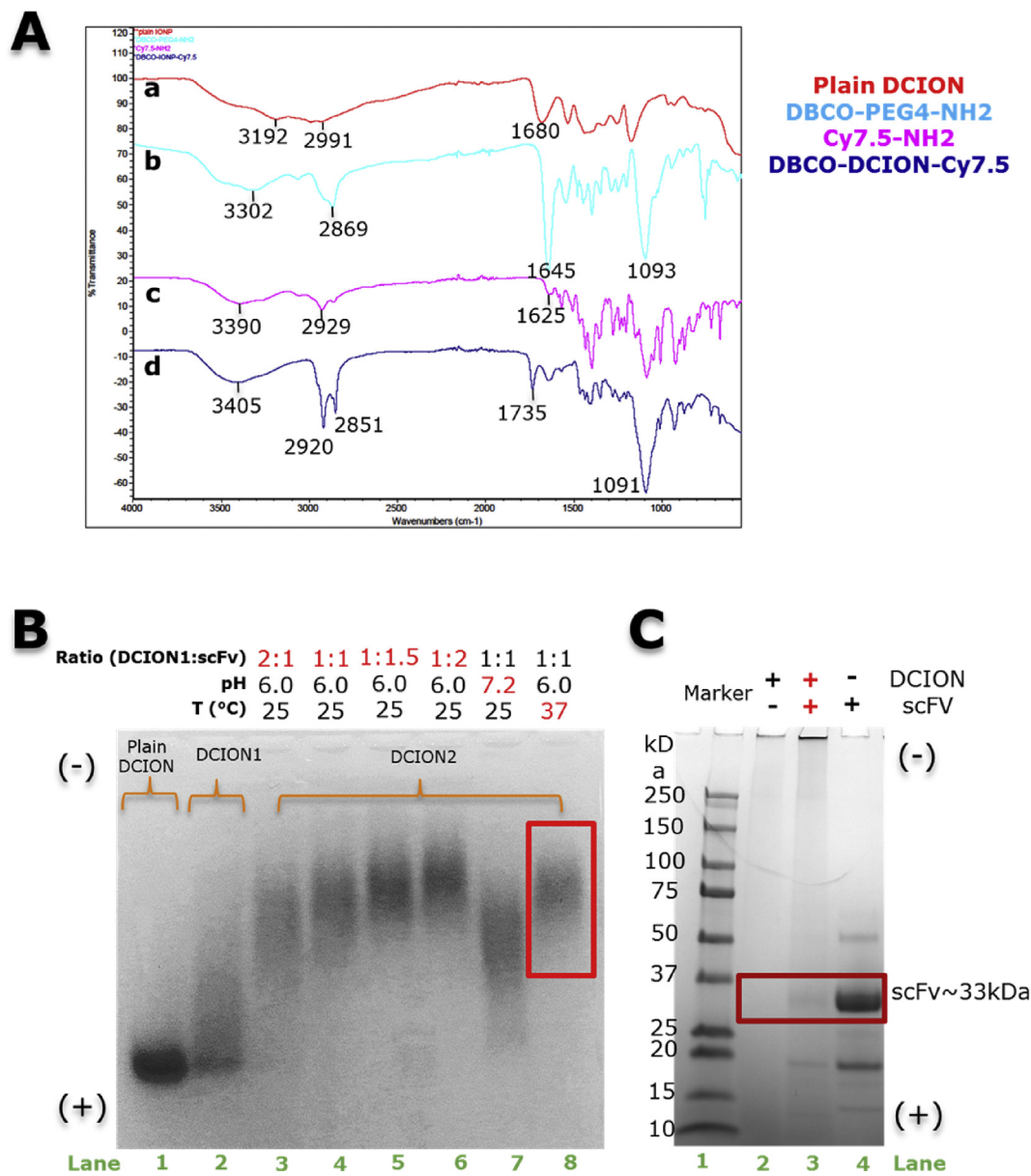

Fig. 2. **Successful conjugation of DCIONs with NIR dyes and scFv. (A)** Transform infrared spectroscopy (FTIR) spectra showing successful conjugation of NH$_2$-PEG$_4$-DBCO and NH$_2$-Cy7.5 to DCIONs via carbodiimide reaction. **(B)** Agarose gel showing the DCIONs before and after conjugation with scFv at different conditions. Reaction condition on lane 8 was chosen as optimum condition and was used for later experiment. **(C)** SDS-PAGE gel showing the scFv in the reaction mixture after click conjugation. A 33-kDa band representing free or non-coupled scFv molecules, is seen on lane 4 (control solution containing scFv alone) but is absent on lane 2 (solution containing DCIONs alone) and nearly disappeared on lane 3 (reaction mixture containing both DCION and scFv). Due to their large size, DCIONs could not run through the gel and stuck in the wells.
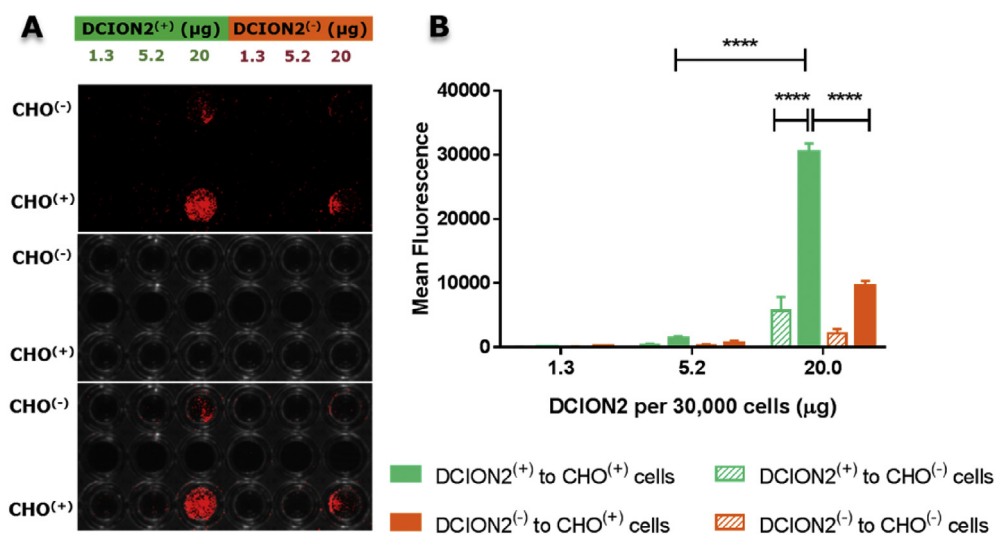
Fig. 3. Binding of DCION2$^{(+)}$ to CHO cells expressing GPIIb/IIIa. (A) Fluorescence, X-ray and overlaid images (top, middle and bottom, respectively) of 96-well plate showing the strong binding of targeted particles DCION2$^{(+)}$ and the weak binding of the control particles DCION2$^{(-)}$ to CHO$^{(+)}$ cells at different particle concentrations. The images also demonstrates the lack of binding of both targeted and non-targeted particles to CHO$^{(-)}$, the cells expressing non-activated receptors. Particles were labelled with NIR dyes which appear as red in the images. X-ray image was used to localize the wells. **(B)** Graph illustrating the binding of DCIONs to two CHO cell lines at various DCION2 concentrations. The groups were compared using two-way ANOVA with Bonferroni post-test (mean ± SEM; ****$P < 0.0001$; n = 3). DCION2$^{(+)}$ indicates scFv$_{antiGPIIb/IIIa}$ conjugated nanoparticles. DCION2$^{(-)}$ indicates scFv$_{mut}$ conjugated nanoparticles. CHO$^{(+)}$ indicated CHO cells expressing activated GPIIb/IIIa receptors. CHO$^{(-)}$ indicates CHO cells expressing non-activated GPIIb/IIIa receptors. (For interpretation of the references to colour in this figure legend, the reader is referred to the web version of this article.)

$r_2/r_1 = 13.8$). Although the r_1 of DCION was reduced at high magnetic field strength, it was higher than those from clinically-used Gd-DTPA and iron oxide SHU-555C. Generally, at all magnetic field strengths considered, DCIONs showed superior relaxivities r_1 and r_2 compared to Gd-DTPA. The results demonstrate the great potential of DCIONs as dual contrast agents. In addition, due to their superior T_1 contrast effect compared to Gd-based agents, DCIONs can be a more sensitive alternative to traditional Gd-based contrast agents for MRI.

3.2. Functionalization of DCIONs with near-infrared (NIR) dye and single-chain antibody

The conjugation procedures are outlined in Scheme 1. NIR fluorescence molecules (Cy7.5-NH$_2$) and DBCO moieties (DBCO-PEG$_4$-NH$_2$) were first introduced onto the DCION surface using carbodiimide crosslinking between primary amino groups from Cy7.5-NH$_2$ and DBCO-PEG$_4$-NH$_2$ and carboxyl groups from DCIONs. The labelled product is called DCION1. The conjugation was successful as demonstrated in Fig. 2A. The FTIR spectrum of non-functionalized DCIONs (a) shows peaks at 3192 cm^{-1} due to O—H stretching of COOH, at 2991 cm^{-1} corresponding to C—H stretching vibrations from the polymer backbone, and at 1680 cm^{-1} attributed to the C=O of carboxyl groups. FTIR spectra of pure DBCO-PEG$_4$-NH$_2$ (b) and pure Cy7.5-NH$_2$ (c) show peaks at 3302 and 3390 cm^{-1} respectively due to N—H stretching vibrations; and at 1645 and 1625 cm^{-1} respectively due to N—H bend vibrations from the primary amine structure.
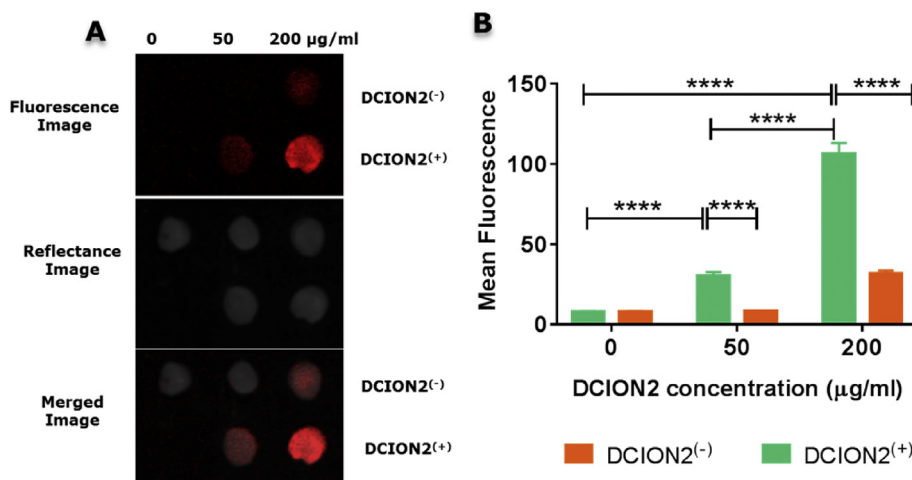

Fig. 4. Specific binding of scFv-coupled particles to *in vitro* human thrombi. (A) Fluorescence, reflectance and merged images showing the good binding of targeted particles DCION2$^{(+)}$ and the low binding of non-targeted particles DCION2$^{(-)}$ to the thrombi. **(B)** Graph illustrating the binding of the particles to the thrombi incubated with different concentrations of particles. The groups were compared using two-way ANOVA with Bonferroni post-test (mean ± SEM; ****$P < 0.0001$; n = 3). DCION2$^{(+)}$ indicates scFv$_{antiGPIIb/IIIa}$ conjugated nanoparticles. DCION2$^{(-)}$ indicates scFv$_{mut}$ conjugated nanoparticles.

In the case of Cy7.5- and DBCO-conjugated DCIONs (DCION1) (d), new peaks at 1735 cm^{-1} and 3405 cm^{-1} appeared, which are attributed to C=O stretching and N−H stretching vibrations from the newly formed amide −CO−NH−, demonstrating the successful coupling of carboxyl groups from DCIONs and amino groups from Cy7.5-NH$_2$ and DBCO-PEG$_4$-NH$_2$. The FTIR spectrum of DCION1 also showed two peaks at 2920 and 2851 cm^{-1}, which represented C−H stretching vibrations from PEG of DBCO-PEG$_4$-NH$_2$, and C−H stretching vibrations from Cy7.5-NH$_2$ molecules, respectively. A new peak at 1091 cm^{-1} was also observed in the spectrum of DCION1, which is due to C−O stretching vibrations of PEG$_4$. These data confirm the successful coupling of DCION with Cy7.5-NH$_2$ and DBCO-PEG$_4$-NH$_2$.

The successful labelling of DCIONs with Cy7.5 and DBCO was also demonstrated by the gel electrophoresis results presented in Fig. 2B where DCION1 (lane 2) appeared to move slower to the positive electrode compared to non-functionalized DCIONs (lane 1). It resulted in the broader band of DCION1 on the gel. This was due to the less negative charge and the larger size of DCION1 after conjugation, which was confirmed by DLS (Table S1).

In the second step of the conjugation procedure, azide (N$_3$) group was site-specifically introduced to the C-terminus of the scFv via enzymatic bioconjugation employing the transpeptidase Sortase A. Enzymatic coupling is increasingly used as an attractive engineering tool for protein modification as it can generate high yields while proceeding under mild conditions. Among other approaches [52], Sortase A enzyme from *Staphylococcus aureus* has been extensively used to immobilize proteins or antibodies to solid surfaces such as polystyrene beads [53], biosensor chips [54], microspheres [55], PET imaging agents [56], iron oxide particles [57], and live cells [57,58]; or to synthesize neoglycoconjugates [59]. The enzyme recognizes substrate proteins containing a short recognition motif LPXTG, cleaves the peptide between threonine (T) and glycine (G) and forms a new bond with nucleophiles containing N-terminal glycine residues [52,57]. The typical yield for this reaction is up to 90% as reported in our previous study [39].

Next, we tagged DCION1 with a single-chain antibody (scFv) via the copper-free click reaction (strain-promoted alkyne-azide cycloaddition − SPAAC) between DBCO groups of the nanoparticle and C-terminal azide group (N$_3$) of the scFv and assessed the efficacy by gel electrophoresis. To optimise the conjugation, we performed this reaction at different conditions using various molar ratios of DCION1 and scFv; different solution pH; and different temperatures. The scFv-tagged DCION1 was named as DCION2. Fig. 2B shows the successful ligation of scFv and DCION1 as demonstrated by the decreased mobility of the nanoparticles (lanes 3−8) through agarose gel due to the formation of larger scFv-DCION1 constructs (DCION2). Smaller ratios of DCION1 to scFv resulted in the bands closer to negative electrode since more scFv molecules were coupled onto the nanoparticles, leading to larger nanoparticle sizes. It was observed that conjugation at pH 7 led to a broader band of DCION2 (lane 7) on the gel as compared to the sample with pH 6 (lane 4), suggesting a lower conjugation efficiency at this pH. DCION2 from the reaction at 37 °C (lane 8) showed a sharper band which was closer to the negative electrode, indicating a more efficient conjugation at this temperature. From this optimization study, we chose the reaction protocol from lane 8 to produce DCION2 for all later experiments.

Fig. 2C also confirms the successful and highly efficient copper-free click coupling reaction between scFv and DCION1. The reaction mixture was loaded on a 12% SDS-PAGE gel. Since DCIONs could not run through the gel due to its small pore size, most of the nanoparticles stayed in the wells, while non-conjugated scFvs could move across the gel and appeared as black bands at 33 kDa on the gel. Lane 2 was from the solution containing only DCIONs, thus there was no band at 33 kDa. Lane 4 was from the reaction mixture absent of DCIONs, therefore all scFvs were non-conjugated and showed up as a strong black band at 33 kDa. Lane 3 shows a very light band at 33 kDa, indicating that most scFvs was conjugated to the particles. Using SDS-PAGE, we could estimate the conjugation efficiency (Fig. S2). Approximately 94% of the scFv in the reaction mixture was successfully coupled to the particles.

3.3. Static adhesion immunofluorescence assay

DCIONs functionalized with scFv$_{antiGPIIb/IIIa}$ was designated as DCION2$^{(+)}$. A mutant variant scFv$_{mut}$ not binding to activated platelet receptors was used as a control. DCIONs functionalized
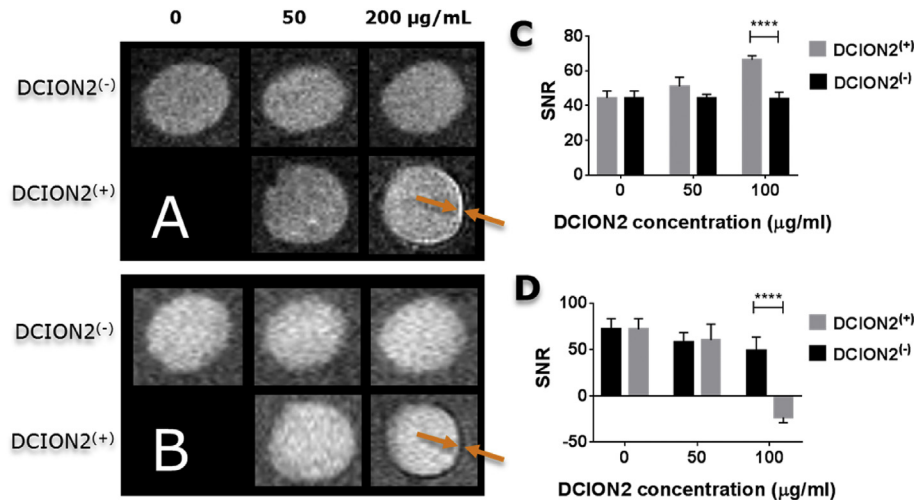

Fig. 5. *In vitro* human thrombus binding assay. (A) T$_1$-weighted and (B) T$_2$-weighted MR images of thrombi incubated with DCIONs for 15 min at different concentrations under a 9.4 T MRI. DCION2$^{(+)}$ indicates scFv$_{antiGPIIb/IIIa}$ conjugated nanoparticles. DCION2$^{(−)}$ indicates scFv$_{mut}$ conjugated nanoparticles. Orange arrows point to the white ring (5A) and the black ring (5B) surrounding the thrombus as the results of signal enhancement and signal diminishment in T$_1$- and T$_2$-weighted imaging, respectively, which is due to the binding of DCION2$^{(+)}$ on the surface of the thrombus. Thrombus incubated with a low concentration of DCION2$^{(+)}$ (50 μg/mL) did not have any obvious white or black ring around it. (C) Graph plotting T$_1$-weighted signal-to-noise-ratio of thrombus edge. (D) Graph plotting T$_2$-weighted signal-to-noise-ratio of thrombus edge. (For interpretation of the references to colour in this figure legend, the reader is referred to the web version of this article.)

with control scFv was called DCION2$^{(-)}$. CHO cell lines expressing the activated and non-activated GPIIb/IIIa receptors were used in this immunofluorescence experiments with DCION2 constructs. Using PAC-1 (BD Biosciences), a commercial antibody for activated GPIIb/IIIa, we confirmed that we had both CHO cells expressing activated GPIIb/IIIa receptors (CHO$^{(+)}$) and those expressing non-activated receptors (CHO$^{(-)}$) (Fig. S3D). Flow cytometry also proved that scFv$_{antiGPIIb/IIIa}$ was able to bind to CHO$^{(+)}$, but not to CHO$^{(-)}$ (Fig. S3A). Control scFv$_{mut}$ could not bind to either activated or non-activated GPIIb/IIIa expressing CHO cells, (Fig. S3B). Anti-V5 pAb labelled with FITC was used in the flow cytometer assay to visualize the binding scFv to the cells as it can bind specifically to the V5 tag on the scFv molecules. Fig. S3C illustrated the lack of binding of anti-V5 pAb to both cell lines.
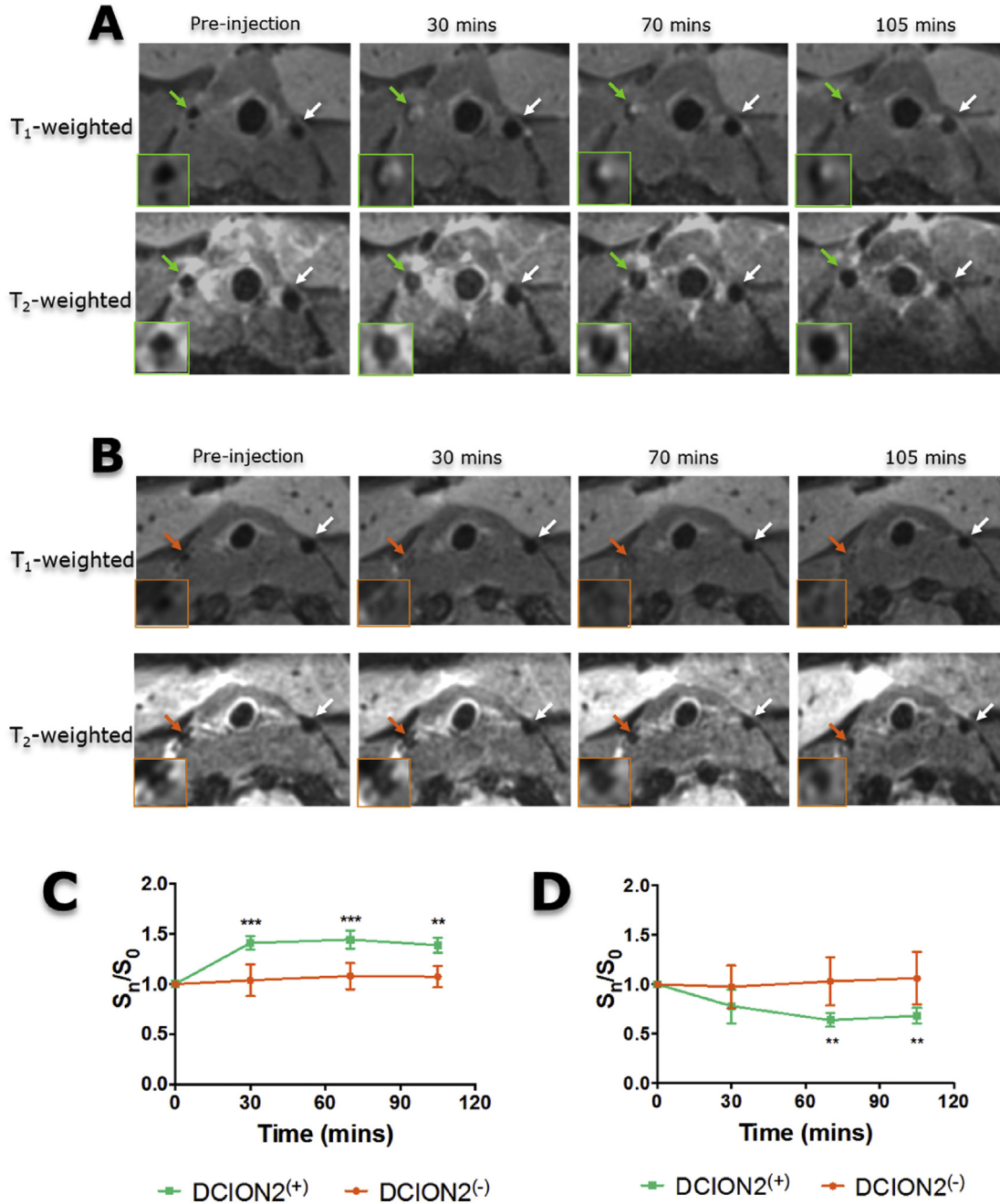

Fig. 6. *In vivo* MRI of carotid artery thrombus before and after administration of scFv-coupled dual contrast iron oxide nanoparticles at 7 T magnetic field strength. (A) and (B) Transverse sections showing T$_1$- and T$_2$-weighted MR images of carotid arteries from mice administered with DCION2$^{(+)}$ and DCION2$^{(-)}$, respectively. Right carotid artery was injured (green arrow: arteries with DCION2$^{(+)}$, orange arrow: arteries with DCION2$^{(-)}$) and left carotid artery was not injured (white arrow). Inset images represents enlarged views of the injured arteries. After injection of DCION2$^{(+)}$, there was a signal enhancement in T$_1$ image and a signal drop in T$_2$ image compared with pre-injection images and the uninjured left carotid artery, indicating DCION2$^{(+)}$ binding. There was no noticeable change in both T$_1$ and T$_2$ images of mouse injected with DCION2$^{(-)}$ before and after injection. Normal carotid arteries showed black in both T$_1$- and T$_2$-weighted MRI due to the flow effect. (C) and (D) Graphs representing the change of T$_1$-weighted and T$_2$-weighted signals, respectively, at different time points. The groups were compared using repeated-measurements ANOVA over time with Bonferroni post-test at each time point (mean ± SEM; **$P < 0.005$, ***$P < 0.0005$; n = 4). DCION2$^{(+)}$ indicates scFv$_{antiGPIIb/IIIa}$ conjugated nanoparticles. DCION2$^{(-)}$ indicates scFv$_{mut}$ conjugated nanoparticles. (For interpretation of the references to colour in this figure legend, the reader is referred to the web version of this article.)
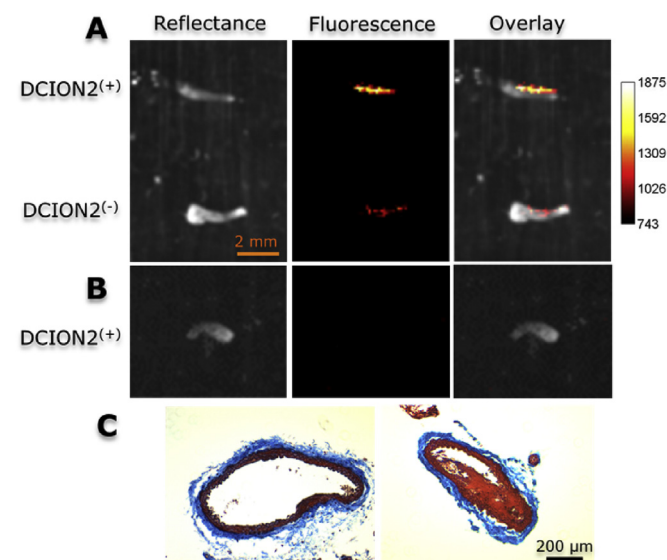
Fig. 7. Ex vivo validation of particle binding and thrombus formation. (A) Reflectance, fluorescence and overlaid images of the injured carotid arteries showing the strong, specific binding of DCION2$^{(+)}$ and the low, non-specific binding of DCION2$^{(-)}$ to thrombosis. **(B)** Reflectance, fluorescence and overlaid images of the normal carotid artery showing the non-binding of DCION2$^{(+)}$. **(C)** Histochemistry of an uninjured carotid artery (left) and an injured carotid artery with wall-adherent thrombus (right). The thrombus area appears red in the histochemistry (Masson's trichrome staining). DCION2$^{(+)}$ indicates scFv$_{antiGPIIb/IIIa}$ conjugated nanoparticles. DCION2$^{(-)}$ indicates scFv$_{mut}$ conjugated nanoparticles. (For interpretation of the references to colour in this figure legend, the reader is referred to the web version of this article.)

In the adhesion assays, DCION2$^{(+)}$ bound specifically to activated GPIIb/IIIa CHO cells. Fig. 3 shows a significantly higher numbers of DCION2$^{(+)}$ binding to CHO$^{(+)}$ cells compared with CHO$^{(-)}$ cells, demonstrated by a higher fluorescence signal detected from the well containing CHO$^{(+)}$ and DCION2$^{(+)}$. Increasing the nanoparticles in the incubation medium resulted in higher fluorescence intensities or more binding particles. Non-targeted DCION2$^{(-)}$ also bound more to CHO$^{(+)}$ cells than to CHO$^{(-)}$ cells, but significantly lower than the targeted DCION2$^{(+)}$. These data confirmed the preserved functionality of scFv$_{antiGPIIb/IIIa}$ after conjugation onto the nanoparticles.

3.4. In vitro human thrombus adhesion assay and MR imaging

The targeting of scFv$_{antiGPIIb/IIa}$ to activated GPIIb/IIIa receptors on platelets was tested and it was concluded that after the introduction of azide N_3 to the C-terminus of the scFv, its binding functionality was preserved (Fig. S4A). The control scFv$_{mut}$ and the secondary antibody anti-V5 pAb did not show binding to both non-activated and activated platelets (Figs. S4B and C). The adhesion of targeted and non-targeted nanoparticles to in vitro human thrombi was assessed using different concentrations of nanoparticles. As can be seen in Fig. 4, DCION2$^{(+)}$ bound significantly to the thrombus at all concentrations, compared with DCION2$^{(-)}$. MR imaging of the thrombi was performed and showed excellent magnetic resonance contrast properties of our nanoparticles in both T_1- and T_2-weighted imaging (Fig. 5). The binding of DCION2$^{(+)}$ on the surface of the thrombus was demonstrated by a bright/white ring around the thrombi in T_1-weighted images; and by a dark/black ring around the thrombi in T_2-weighted images. Since the ultra-small nanoparticles only attached to the surface of the thrombus in this experiment, signal enhancement or diminishment only happened on the surface of the thrombus, resulting in a thin and white ring or a thin and black ring surrounding the thrombus. The higher the

number of nanoparticles in the incubation medium, the stronger the signal enhancement around the thrombus surface in the T_1-imaging, and the stronger the signal diminishment around the thrombus surface in T_2-imaging (Fig. S5). At very high concentrations of DCION2$^{(+)}$, susceptibility artefacts appeared around the thrombus due to the accumulation of a large number of iron oxide nanoparticles on the thrombus surface. Our data are in agreement with those from other studies which showed that at high concentration, ultra-small superparamagnetic iron oxide nanoparticles could cause signal loss in T_1-weighted imaging [60,61]. The same result was observed for gadolinium-based contrast agents [62—64]. These susceptibility artefacts have been attributed to T_2*-shortening effects from high concentrations of gadolinium or ultra-small iron oxide nanoparticles, leading to signal loss.

3.5. In vivo MR imaging and histology

To investigate the capacity for targeting and imaging of DCION2$^{(+)}$ in vivo, we used C57BL/6 wild-type mice at 11 weeks old (approximately 25 g) and performed MR imaging using a preclinical 7 T MRI scanner. For each animal, 0.4 mg of either targeted or non-targeted nanoparticles (0.32 mg Fe per kg mouse) was administered. T_1- and T_2-weighted images of carotid arteries at different time points were collected and shown in Fig. 6A and B. These figures demonstrate signal enhancement in T_1-weighted images and signal decrease in T_2-weighted images of arterial thrombus from mice injected with DCION2$^{(+)}$. Negligible change in image intensity was observed after injection of the non-targeted DCION2$^{(-)}$ constructs. Ratios of after-injection signal and before-injection (baseline) signal are shown in Fig. 6C and D. For both T_1- and T_2-imaging, the largest change in signal occurred at 70 min after injection and then started to decline, which was probably due to washing away of the particles over time. The signal ratios were also found to be significantly different between DCION2$^{(+)}$ and DCION2$^{(-)}$ at this time point for both imaging settings. It is noted that normal carotid arteries showed black in both T_1- and T_2-weighted MRI due to the flow effect.

After MRI, the injured carotid arteries containing thrombi were collected and their NIR fluorescence was imaged. Fig. 7A illustrates the specific binding of DCION2$^{(+)}$ to the thrombus, as demonstrated by a stronger fluorescence signal compared to DCION2$^{(-)}$. Histological analysis of the injured artery confirmed the formation of thrombus in the vessel, which occupied approximately 50—80% of the vessel lumen (Fig. 7B, right image). The uninjured carotid artery was also collected and its histological image shows a lack of thrombus formation (Fig. 7B, left image).

4. Conclusion

In conclusion, the presented data demonstrate a successful and unique approach for MR molecular imaging of thrombosis via a dual mode strategy employing positive and negative contrast iron oxide nanoparticles. DCIONs were functionalized and tagged with scFv using a combination of chemical and biological techniques. The conjugation was achieved with a high yield (94%) and a preserved scFv bioactivity was confirmed. The targeting of scFv$_{antiGPIIb/IIIa}$-tagged DCIONs to activated GPIIb/IIIa receptors was demonstrated in vitro with receptor-expressing CHO cells and with activated platelets. The suitability of our particles for dual modal imaging was demonstrated in MR imaging of both in vitro human thrombus and mouse model of carotid artery thrombosis. Thrombi were highlighted in T_1-weighted imaging by a bright/positive signal and in T_2-weighted imaging by a dark/negative signal generated around the surface of the thrombus by the presence of the DCIONs. Binding of DCIONs to the thrombi was confirmed by fluorescence

imaging of the injured carotid arteries collected after *in vivo* MRI experiments. These results demonstrate retention of targeting capability of our conjugated constructs *in vivo*. Both T_1- and T_2-images can be recorded simultaneously which enables self-confirmation of images and leads to a greater diagnostic accuracy. The duality of T_1 and T_2 is particularly important for intravascular thrombosis imaging, which is otherwise difficult to achieve if using widely-studied negative-contrast iron oxide nanoparticles providing a "black" contrast in a black vessel background. These nanoparticles also have potential to replace traditional gadolinium-based contrast materials due to their stronger T_1 contrast effect, compared to the gadolinium-based agents. The use of these nanoparticles can potentially bring the validity of MR imaging for cardiovascular disease to a higher level. Its utility is broad and not limited to imaging of thrombotic, atherosclerotic, and inflammatory diseases, but can also be applied to other biological targets with enhanced reliability.

Acknowledgements

Appendix A. Supplementary data

Supplementary data related to this article can be found at http://dx.doi.org/10.1016/j.biomaterials.2017.04.037.

Notes

The authors declare no competing financial interest. K.P. is inventor on patents describing scFvs directed against activated GPIIb/IIIa.

References

[1] D. Mozaffarian, E.J. Benjamin, A.S. Go, D.K. Arnett, M.J. Blaha, M. Cushman, et al., Heart disease and stroke statistics — 2015 update, Circulation 131 (2015) e30—e320.

[2] G.J. Strijkers, Targeted nanoparticle for cardiovascular molecular imaging, Curr. Radiol. Rep. 1 (2013) 191—204.

[3] G.K. Hansson, Inflammation, atherosclerosis, and coronary artery disease, N. Engl. J. Med. 352 (2005) 1685—1695.

[4] M.C. Kramer, S.Z. Rittersma, R.J. de Winter, E.R. Ladich, D.R. Fowler, Y.H. Liang, et al., Relationship of thrombus healing to underlying plaque morphology in sudden coronary death, J. Am. Coll. Cardiol. 55 (2010) 122—132.

[5] K.L. Ciesienski, P. Caravan, Molecular MRI of thrombosis, Curr. Cardiovasc Imaging Rep. 4 (2010) 77—84.

[6] D. von Elverfeldt, A. Maier, D. Duerschmied, M. Braig, T. Witsch, X. Wang, et al., Dual-contrast molecular imaging allows noninvasive characterization of myocardial ischemia/reperfusion injury after coronary vessel occlusion in mice by magnetic resonance imaging, Circulation 130 (2014) 676—687.

[7] S. Yokoyama, H. Ikeda, N. Haramaki, H. Yasukawa, T. Murohara, T. Imaizumi, Platelet P-selectin plays an important role in arterial thrombogenesis by forming large stable platelet-leukocyte aggregates, J. Am. Coll. Cardiol. 45 (2005) 1280—1286.

[8] M.F. Kircher, U. Mahmood, R.S. King, R. Weissleder, L. Josephson, A multimodal nanoparticle for preoperative magnetic resonance imaging and intraoperative optical brain tumor delineation, Cancer Res. 63 (2003) 8122—8125.

[9] M. Nahrendorf, H. Zhang, S. Hembrador, P. Panizzi, D.E. Sosnovik, E. Aikawa, et al., Nanoparticle PET-CT imaging of macrophages in inflammatory atherosclerosis, Circulation 117 (2008) 379—387.

[10] J. Cheon, J.H. Lee, Synergistically integrated nanoparticles as multimodal probes for nanobiotechnology, Acc. Chem. Res. 41 (2008) 1630—1640.

[11] J. Gao, H. Gu, B. Xu, Multifunctional magnetic nanoparticles: design, synthesis, and biomedical applications, Acc. Chem. Res. 42 (2009) 1097—1107.

[12] A. Phinikaridou, M.E. Andia, S. Lacerda, S. Lorrio, M.R. Makowski, R.M. Botnar, Molecular MRI of atherosclerosis, Molecules 18 (2013) 14042—14069.

[13] Z. Li, P.W. Yi, Q. Sun, H. Lei, H.L. Zhao, Z.H. Zhu, et al., Ultrasmall water-soluble and biocompatible magnetic iron oxide nanoparticles as positive and negative dual contrast agents, Adv. Funct. Mater. 22 (2012) 2387—2393.

[14] J.W. Bulte, D.L. Kraitchman, Iron oxide MR contrast agents for molecular and cellular imaging, NMR Biomed. 17 (2004) 484—499.

[15] A. Phinikaridou, M.E. Andia, A. Protti, A. Indermuehle, A. Shah, A. Smith, et al., Noninvasive magnetic resonance imaging evaluation of endothelial permeability in murine atherosclerosis using an albumin-binding contrast agent, Circulation 126 (2012) 707—719.

[16] M.R. Makowski, A.J. Wiethoff, U. Blume, F. Cuello, A. Warley, C.H. Jansen, et al., Assessment of atherosclerotic plaque burden with an elastin-specific magnetic resonance contrast agent, Nat. Med. 17 (2011) 383—388.

[17] P.M. Winter, A.M. Neubauer, S.D. Caruthers, T.D. Harris, J.D. Robertson, T.A. Williams, et al., Endothelial alpha(v)beta3 integrin-targeted fumagillin nanoparticles inhibit angiogenesis in atherosclerosis, Arterioscler. Thromb. Vasc. Biol. 26 (2006) 2103—2109.

[18] J.A. Ronald, J.W. Chen, Y. Chen, A.M. Hamilton, E. Rodriguez, F. Reynolds, et al., Enzyme-sensitive magnetic resonance imaging targeting myeloperoxidase identifies active inflammation in experimental rabbit atherosclerotic plaques, Circulation 120 (2009) 592—599.

[19] X. Yu, S.K. Song, J. Chen, M.J. Scott, R.J. Fuhrhop, C.S. Hall, et al., High-resolution MRI characterization of human thrombus using a novel fibrin-targeted paramagnetic nanoparticle contrast agent, Magn. Reson Med. 44 (2000) 867—872.

[20] S. Flacke, S. Fischer, M.J. Scott, R.J. Fuhrhop, J.S. Allen, M. McLean, et al., Novel MRI contrast agent for molecular imaging of fibrin: implications for detecting vulnerable plaques, Circulation 104 (2001) 1280—1285.

[21] R.M. Botnar, A. Buecker, A.J. Wiethoff, E.C. Parsons Jr., M. Katoh, G. Katsimaglis, et al., In vivo magnetic resonance imaging of coronary thrombosis using a fibrin-binding molecular magnetic resonance contrast agent, Circulation 110 (2004) 1463—1466.

[22] R.M. Botnar, A.S. Perez, S. Witte, A.J. Wiethoff, J. Laredo, J. Hamilton, et al., In vivo molecular imaging of acute and subacute thrombosis using a fibrin-binding magnetic resonance imaging contrast agent, Circulation 109 (2004) 2023—2029.

[23] E. Spuentrup, A. Buecker, M. Katoh, A.J. Wiethoff, E.C. Parsons Jr., R.M. Botnar, et al., Molecular magnetic resonance imaging of coronary thrombosis and pulmonary emboli with a novel fibrin-targeted contrast agent, Circulation 111 (2005) 1377—1382.

[24] M.R. Makowski, S.C. Forbes, U. Blume, A. Warley, C.H. Jansen, A. Schuster, et al., In vivo assessment of intraplaque and endothelial fibrin in ApoE(-/-) mice by molecular MRI, Atherosclerosis 222 (2012) 43—49.

[25] M. Sirol, V.V. Itskovich, V. Mani, J.G. Aguinaldo, J.T. Fallon, B. Misselwitz, et al., Lipid-rich atherosclerotic plaques detected by gadofluorine-enhanced in vivo magnetic resonance imaging, Circulation 109 (2004) 2890—2896.

[26] J.C. Frias, K.J. Williams, E.A. Fisher, Z.A. Fayad, Recombinant HDL-like nanoparticles: a specific contrast agent for MRI of atherosclerotic plaques, J. Am. Chem. Soc. 126 (2004) 16316—16317.

[27] M. Nahrendorf, F.A. Jaffer, K.A. Kelly, D.E. Sosnovik, E. Aikawa, P. Libby, et al., Noninvasive vascular cell adhesion molecule-1 imaging identifies inflammatory activation of cells in atherosclerosis, Circulation 114 (2006) 1504—1511.

[28] M.E. Kooi, V.C. Cappendijk, K.B. Cleutjens, A.G. Kessels, P.J. Kitslaar, M. Borgers, et al., Accumulation of ultrasmall superparamagnetic particles of iron oxide in human atherosclerotic plaques can be detected by in vivo magnetic resonance imaging, Circulation 107 (2003) 2453—2458.

[29] V. Amirbekian, M.J. Lipinski, K.C. Briley-Saebo, S. Amirbekian, J.G. Aguinaldo, D.B. Weinreb, et al., Detecting and assessing macrophages in vivo to evaluate atherosclerosis noninvasively using molecular MRI, Proc. Natl. Acad. Sci. U. S. A. 104 (2007) 961—966.

[30] C. von zur Muhlen, D. von Elverfeldt, J.A. Moeller, R.P. Choudhury, D. Paul, C.E. Hagemeyer, et al., Magnetic resonance imaging contrast agent targeted toward activated platelets allows in vivo detection of thrombosis and monitoring of thrombolysis, Circulation 118 (2008) 258—367.

[31] C. von zur Muhlen, K. Peter, Z.A. Ali, J.E. Schneider, M.A. McAteer, S. Neubauer, et al., Visualization of activated platelets by targeted magnetic resonance imaging utilizing conformation-specific antibodies against glycoprotein IIb/IIIa, J. Vasc. Res. 46 (2009) 6—14.

[32] C. von Zur Muhlen, D. von Elverfeldt, R.P. Choudhury, J. Ender, I. Ahrens, M. Schwarz, et al., Functionalized magnetic resonance contrast agent selectively binds to glycoprotein IIb/IIIa on activated human platelets under flow conditions and is detectable at clinically relevant field strengths, Mol. Imaging 7 (2008) 59—67.

[33] M. Gawaz, H. Langer, A.E. May, Platelets in inflammation and atherogenesis, J. Clin. Invest. 115 (2005) 3378—3384.

[34] P. von Hundelshausen, C. Weber, Platelets as immune cells: bridging inflammation and cardiovascular disease, Circ. Res. 100 (2007) 27—40.

[35] J.D. Hohmann, X. Wang, S. Krajewski, C. Selan, C.A. Haller, A. Straub, et al., Delayed targeting of CD39 to activated platelet GPIIb/IIIa via a single-chain antibody: breaking the link between antithrombotic potency and bleeding?

Blood 121 (2013) 3067—3075.

[36] M. Schwarz, Y. Katagiri, M. Kotani, N. Bassler, C. Loeffler, C. Bode, et al., Reversibility and persistence of GPIIb/IIIa blocker-induced conformational change of GPIIb/IIIa (CD41/CD61), J. Pharmacol. Exp. Ther. 308 (2004) 1002—1011.

[37] H. Ta, S. Prabhu, E. Leitner, F. Jia, D. von Elverfeldt, K. Jackson, et al., Enzymatic single-chain antibody tagging: a universal approach to targeted molecular imaging and cell homing in cardiovascular disease, Circ. Res. 109 (2011) 365—373.

[38] K. Alt, B.M. Paterson, E. Westein, S.E. Rudd, S.S. Poniger, S. Jagdale, et al., Aversatile approach for the site-specific modification of recombinant antibodies using a combination of enzyme-mediated bioconjugation and click chemistry, Angew. Chem. Int. Ed. 54 (2015) 1—6.

[39] B.M. Paterson, K. Alt, C.M. Jeffery, R.I. Price, S. Jagdale, S. Rigby, et al., Enzyme-mediated site-specific bioconjugation of metal complexes to proteins: sortase-mediated coupling of Copper-64 to a single-chain antibody, Angew. Chem. Int. Ed. 53 (2014) 6115—6119.

[40] P. Stoll, N. Bassler, C.E. Hagemeyer, S.U. Eisenhardt, Y.C. Chen, R. Schmidt, et al., Targeting ligand-induced binding sites on GPIIb/IIIa via single-chain antibody allows effective anticoagulation without bleeding time prolongation, Arterioscler. Thromb. Vasc. Biol. 27 (2007) 1206—1212.

[41] A. Roch, R.N. Muller, Theory of proton relaxation induced by superparamagnetic particles, J. Chem. Phys. 110 (1999) 5403—5411.

[42] U.I. Tromsdorf, O.T. Bruns, S.C. Salmen, U. Beisiegel, H. Weller, A highly effective, nontoxic T_1 MR contrast agent based on ultrasmall PEGylated iron oxide nanoparticles, Nano Lett. 9 (2009) 4434—4440.

[43] B.H. Kim, N. Lee, H. Kim, K. An, Y.I. Park, Y. Choi, et al., Large-scale synthesis of uniform and extremely small-sized iron oxide nanoparticles for high-resolution T_1 magnetic resonance imaging contrast agents, J. Am. Chem. Soc. 133 (2011) 12624—12631.

[44] F. Hu, Q. Jia, Y. Li, M. Gao, Facile synthesis of ultrasmall PEGylated iron oxide nanoparticles for dual-contrast T_1- and T_2-weighted magnetic resonance imaging, Nanotechnology 22 (2011) 245604—245611.

[45] N. Pothayee, N. Pothayee, N. Jain, N. Hu, S. Balasubramaniam, L.M. Johnson, et al., Magnetic block ionomer complexes for potential dual imaging and therapeutic agents, Chem. Mater. 24 (2012) 2056—2063.

[46] N. Pothayee, S. Balasubramaniam, N. Pothayee, N. Jain, N. Hu, Y. Lin, et al., Magnetic nanoclusters with hydrophilic spacing for dual drug delivery and sensitive magnetic resonance imaging, J. Mater Chem. B 1 (2013) 1142—1149.

[47] E.A. Neuwelt, B.E. Hamilton, C.G. Varallyay, W.R. Rooney, R.D. Edelman, P.M. Jacobs, et al., Ultrasmall superparamagnetic iron oxides (USPIOs): a future alternative magnetic resonance (MR) contrast agent for patients at risk for nephrogenic systemic fibrosis (NSF)? Kidney Int. 75 (2009) 465—474.

[48] Y.X.J. Wang, Superparamagnetic iron oxide based MRI contrast agents: current status of clinical application, Quant. Imaging Med. Surg. 1 (2011) 35—40.

[49] S. Xue, C. Zhang, Y. Yang, L. Zhang, D. Cheng, J. Zhang, et al., 99mTc-Labeled iron oxide nanoparticles for dual-contrast (T1/T2) magnetic resonance and dual-modality imaging of tumor angiogenesis, J. Biomed. Nanotechnol. 11 (2015) 1027—1037.

[50] C.R. Bowers, D.P. Weitekamp, Transformation of symmetrization order to nuclear-spin magnetization by chemical reaction and nuclear magnetic resonance, Phys. Rev. Lett. 57 (1986) 2645—2648.

[51] T. Geelen, L.E. Paulic, B.F. Coolen, K. BNicolay, G.J. Strijkers, Passive targeting of paramagnetic lipid-based contrast agents to acute mouse cardiac ischemia/reperfusion injury, Proc. Int. Soc. Mag. Reson. Med. 19 (2011), 1356-.

[52] H.T. Ta, K. Peter, C.E. Hagemeyer, Enzymatic antibody tagging: toward a universal biocompatible targeting tool, Trends Cardiovasc. Med. 22 (2012) 105—111.

[53] R. Parthasarathy, S. Subramanian, E.T. Boder, Sortase A as a novel molecular "stapler" for sequence-specific protein conjugation, Bioconjug. Chem. 18 (2007) 469—476.

[54] F. Clow, J.D. Fraser, T. Proft, Immobilization of proteins to biacore sensor chips using Staphylococcus aureus sortase A, Biotechnol. Lett. 30 (2008) 1603—1607.

[55] S. Wu, T. Proft, The use of sortase-mediated ligation for the immobilisation of bacterial adhesins onto fluorescence-labelled microspheres: a novel approach to analyse bacterial adhesion to host cells, Biotechnol. Lett. 32 (2010) 1713—1718.

[56] K. Alt, B.M. Paterson, E. Westein, S.E. Rudd, S.S. Poniger, S. Jagdale, et al., A versatile approach for the site-specific modification of recombinant antibodies using a combination of enzyme-mediated bioconjugation and click chemistry, Angew. Chem. Int. Ed. Engl. 54 (2015) 7515—7519.

[57] H.T. Ta, S. Prabhu, E. Leitner, F. Jia, D. von Elverfeldt, K.E. Jackson, et al., Enzymatic single-chain antibody tagging: a universal approach to targeted molecular imaging and cell homing in cardiovascular disease, Circ. Res. 109 (2011) 365—373.

[58] T. Tanaka, T. Yamamoto, S. Tsukiji, T. Nagamune, Site-specific protein modification on living cells catalyzed by Sortase, Chembiochem 9 (2008) 802—807.

[59] S. Samantaray, U. Marathe, S. Dasgupta, V.K. Nandicoori, R.P. Roy, Peptide-sugar ligation catalyzed by transpeptidase sortase: a facile approach to neo-glycoconjugate synthesis, J. Am. Chem. Soc. 130 (2008) 2132—2133.

[60] G. Fananapazir, D. Marin, P.V. Suhocki, C.Y. Kim, M.R. Bashir, Vascular artifact mimicking thrombosis on MR imaging using ferumoxytol as a contrast agent in abdominal vascular assessment, J. Vasc. Interv. Radiol. 25 (2014) 969—976.

[61] S.R. Alam, C. Stirrat, J. Richards, S. Mirsadraee, S.I. Semple, G. Tse, et al., Vascular and plaque imaging with ultrasmall superparamagnetic particles of iron oxide, J. Cardiovasc Magn. Reson. 17 (2015) 83.

[62] V.S. Lee, D.J. Martin, G.A. Krinsky, N.M. Rofsky, Gadolinium-enhanced MR angiography: artifacts and pitfalls, AJR Am. J. Roentgenol. 175 (2000) 197—205.

[63] A.T. Tirkes, M.A. Rosen, E.S. Siegelman, Gadolinium susceptibility artifact causing false positive stenosis isolated to the proximal common carotid artery in 3D dynamic contrast medium enhanced MR angiography of the thorax—a brief review of causes and prevention, Int. J. Cardiovasc. Imaging 19 (2003) 151—155.

[64] M.A. Neimatallah, T.L. Chenevert, R.C. Carlos, F.J. Londy, Q. Dong, M.R. Prince, et al., Subclavian MR arteriography: reduction of susceptibility artifact with short echo time and dilute gadopentetate dimeglumine, Radiology 217 (2000) 581—586.

Supporting Information to

Molecular Imaging of Activated Platelets via Antibody-Targeted Ultra-small Iron Oxide Nanoparticles Displaying Unique Dual MRI Contrast

<u>Supplementary Materials and Methods</u>

Evaluation of conjugation efficiency

Fourier Transform Infrared Spectroscopy (FTIR): IR spectra of samples was recorded between 500 and 4000 cm^{-1} using Bruker alpha Fourier Transform Infra Red Spectrometer.

SDS-PAGE: 15 µL of sample and 3 µL of 6X reducing SDS loading buffer were added to 1.5-mL tube and incubated at room temperature for 5 min. 18 µL of each sample was loaded and run on SDS-PAGE gel in SDS running buffer at 100V for 1 h. The gel was then stained with Bio-Safe Coomassie Stain (Bio-Rad) for 30 min and subsequently washed with water for 2 h. The gel was visualized and analyzed using a BioRad Gel-Doc system with Image Lab Software (Australia).

Agarose gel electrophoresis: 24 µL of sample containing 0.1 mg DCIONs and 6 µL of 5X loading buffer (without bromophenol blue) were loaded onto a 2% agarose gel. Samples were run on the gel in TAE running buffer at 100V for 1 h. The gel was visualized using a BioRad Gel-Doc system.

Cell culture

All cell culture reagents were obtained from GIBCO/Invitrogen (Australia) unless otherwise noted. Chinese Hamster Ovarian (CHO) cell line attained from the American Type Culture Collection (ATCC). Previously described CHO cell lines stably expressing the activated and non-activated GPIIb/IIIa receptors were used as a reliable test platform for immunofluorescence experiments with scFv-DCION constructs [1-3]. Cells were cultured in Dulbecco's modified Eagle's medium (DMEM) supplemented with 10% fetal bovine serum (FBS), 1% nonessential amino acids (NEAA), 1% penicillin/streptomycin (P/S) and 700 μg/mL Geneticin in a humidified 5% CO_2 atmosphere. A seeding cell population of exponentially-growing cells greater than 95% viability was used for all assays.

Supplementary Tables and Figures

Table S1. Hydrodynamic size and zeta potential of DCIONs before and after conjugation with NIR dyes and scFv-molecules
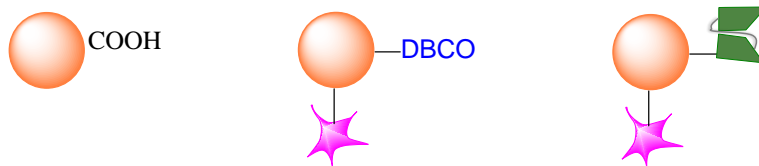
Sample	Plain DCION	DBCO-DCION-Cy7.5 (DCION1)	scFv-DCION-Cy7.5 (DCION2)
Size	7.682 ± 0.235 nm	12.231 ± 1.523 nm	22.652 ± 1.791 nm
PDI	0.231 ± 0.052	0.203 ± 0.058	0.354 ± 0.014
Zeta potential	-40 ± 4.95	-27.5 ± 0.56	-21.4 ± 2.28

Table S2. Relaxivities of dual T_1/T_2 contrast iron oxide nanoparticles reported in literature.

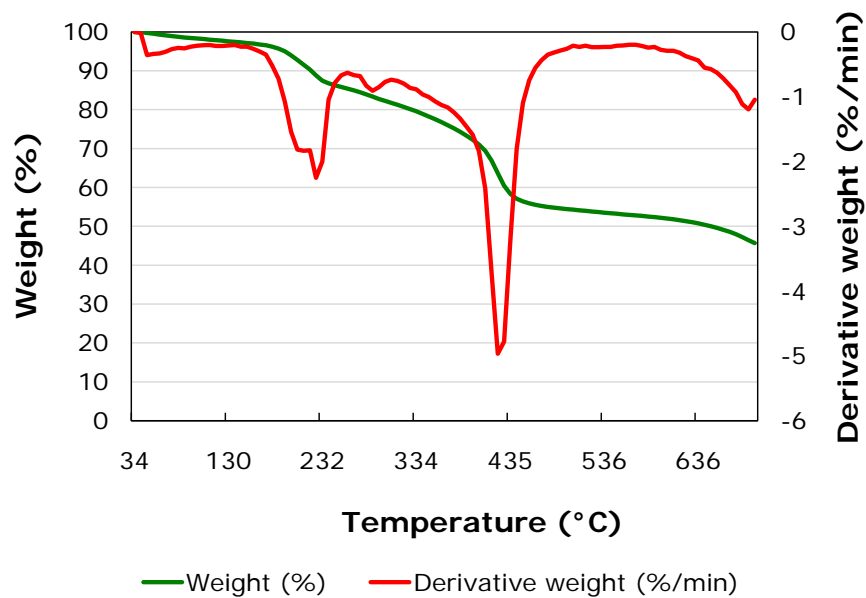| Reference	DCION size (nm)	r_1 (mM^{-1}s^{-1})	r_2 (mM^{-1}s^{-1})	r_2/r_1	Magnetic Field Strength (Tesla)
4	4	7.3	17.52	2.4	1.4
5	3	4.37	29.2	6.12	3
6	5.4	19.7	39.4	2	1.5
7-8	4	18	68	3.8	1.4
9-10	4.8	10	60	6	1.5

Figure S1. TGA curves of DCIONs illustrating two decomposition stages of PMAA-PTTM polymer coated on the nanoparticles
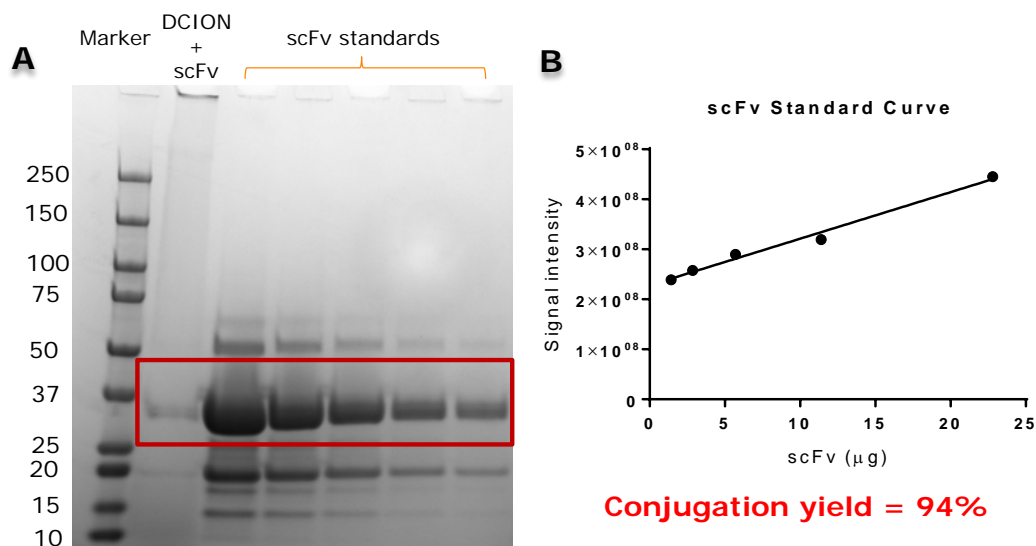
Figure S2. Gel electrophoresis to estimate conjugation efficiency of copper-free click reaction between DCIONs bearing DBCO functional groups and scFv molecules containing azide N_3 groups. (A) SDS-PAGE gel representing protein marker, reaction mixture containing DCIONs and scFv, and solutions containing scFv alone at different concentrations. 33kD bands representing scFv are highlighted in the red box. The disappearing of scFv on lane containing the complete reaction mixture demonstrates the successful conjugation. (B) Graph plotting Coomassie-staining signal intensity generated from scFv at various concentrations.
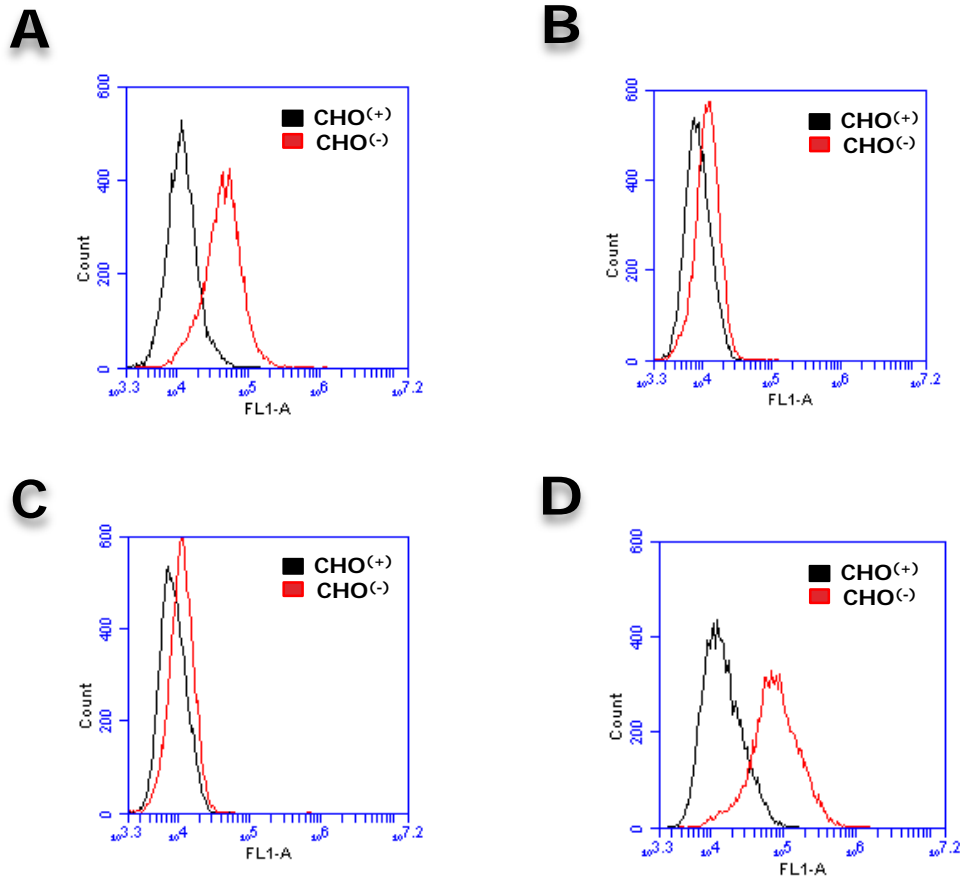
Figure S3. Flow cytometry histograms illustrating binding of scFv-N$_3$ to cells expressing activated GPIIb/IIIa (CHO$^{(+)}$, red histogram) and cells expressing non-activated GPIIb/IIIa (CHO$^{(-)}$, black histogram). (A) Specific binding of scFv$_{antiGPIIb/IIIa}$-N$_3$ to CHO$^{(+)}$ cells and its non-binding to CHO$^{(-)}$ cells. (B) Non-binding of the control scFv$_{mut}$-N$_3$ to both CHO$^{(-)}$ and CHO$^{(+)}$ cells. (C) None binding of the secondary anti-V5 antibody to both CHO$^{(-)}$ and CHO$^{(+)}$. (D) Strong binding of PAC1 to CHO$^{(+)}$ cells and none binding to CHO$^{(-)}$ cells.
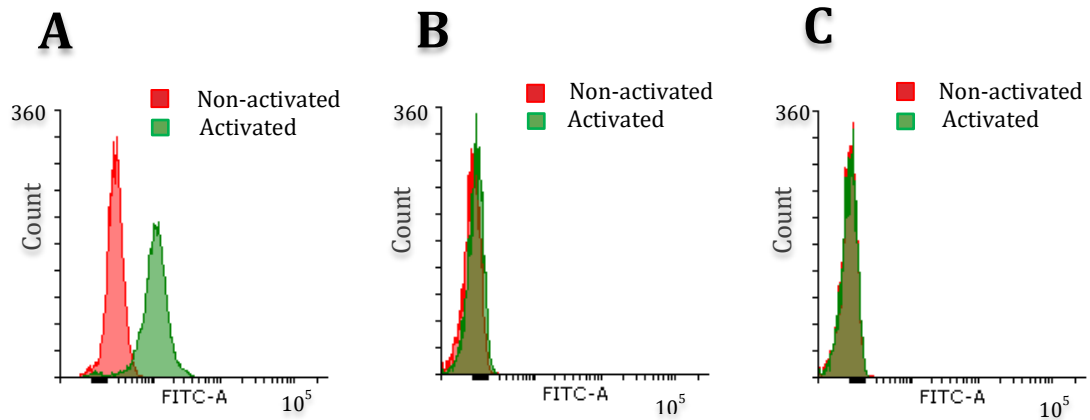
Figure S4. Flow cytometry histograms illustrating binding of scFv-N$_3$ to activated and non-activated GPIIb/IIIa receptors on platelets. (A) Specific binding of scFv$_{antiGPIIb/IIIa}$-N$_3$ to activated platelets and lack of binding to non-activated platelets. (B) Absence of binding of scFv$_{mut}$-N$_3$ to both activated and non-activated platelets. (C) No binding of the secondary anti-V5 antibody alone to activated and non-activated platelets.
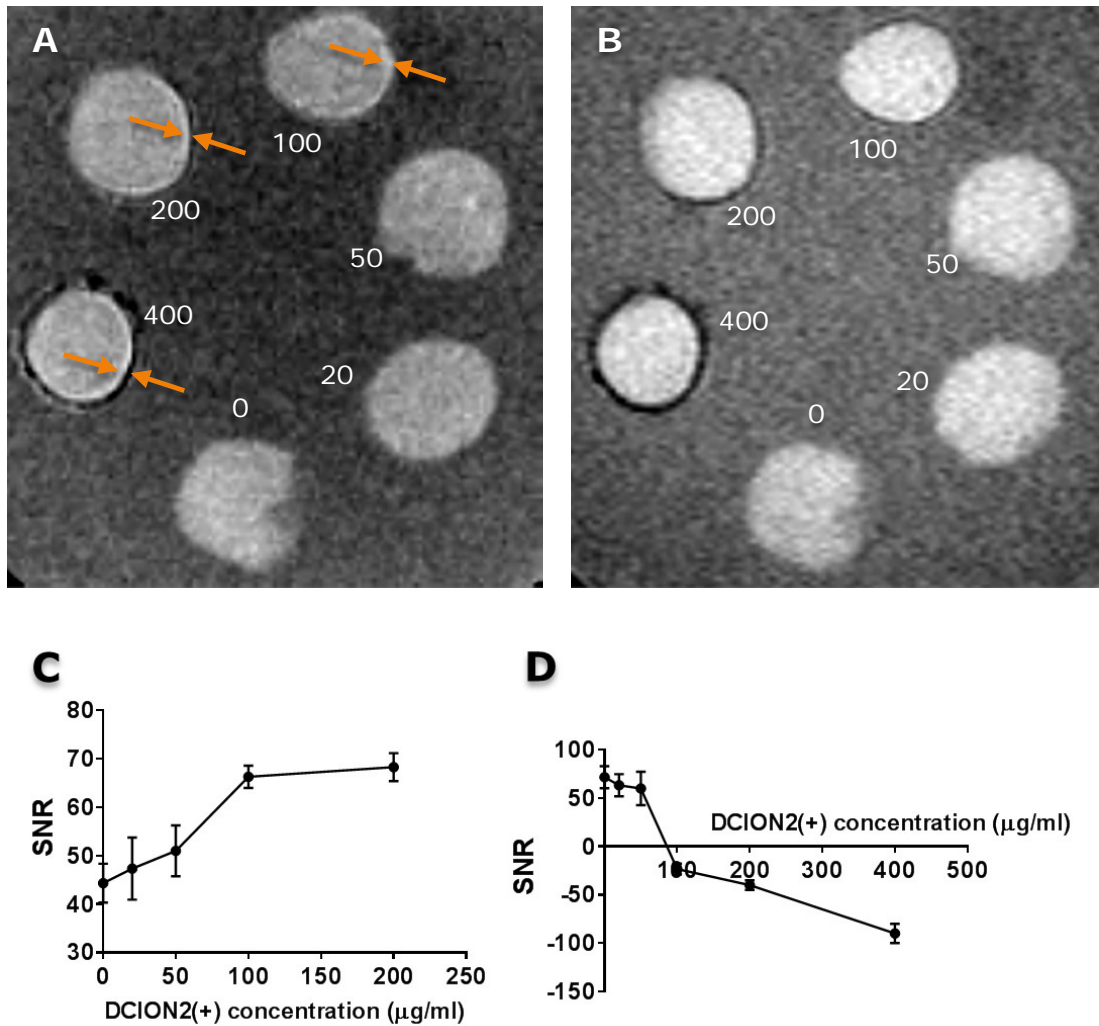
Figure S5. In vitro human thrombus binding assay. (A) T_1-weighted and (B) T_2-weighted images of thrombi incubated with DCION2(+) at different concentrations ranging from 0 to 400 µg/ml under 9.4 Tesla magnetic field strength. Thrombi incubated with the particles at low concentrations (0-50 µg/ml) did not show any difference in the signal. Thrombi incubated with the higher concentrations of the particles (100-400 µg/ml) exhibited thin and bright/white rings (signal enhanced) surrounding the surface of the thrombi in T_1-weighted image, and dark/black rings (signal decreased) surrounding the thrombi in T_2-weighted image. Orange arrows point to the white rings and the black rings on the surface of the thrombi. Thrombus incubated

with very high concentration of the particles (400 µg/ml) appeared to have susceptibility artefacts (dark/black signal) around its surface and outside the white ring in T1-weighted image. (C) Graph plotting T_1-weighted signal-to-noise-ratio of thrombus edge. (D) Graph plotting T_2-weighted signal-to-noise-ratio of thrombus edge.

REFERENCES

1.   Schwarz, M.; Katagiri, Y.; Kotani, M.; Bassler, N.; Loeffler, C.; Bode, C.; Peter, K., Reversibility versus persistence of GPIIb/IIIa blocker-induced conformational change of GPIIb/IIIa (alphaIIbbeta3, CD41/CD61). *The Journal of pharmacology and experimental therapeutics* **2004,** *308* (3), 1002-11.

2.   Stoll, P.; Bassler, N.; Hagemeyer, C. E.; Eisenhardt, S. U.; Chen, Y. C.; Schmidt, R.; Schwarz, M.; Ahrens, I.; Katagiri, Y.; Pannen, B.; Bode, C.; Peter, K., Targeting Ligand-Induced Binding Sites on GPIIb/IIIa via Single-Chain Anibody Allows Effective Anticoagulation Without Bleeding Time Prolongation. *Arterioscler. Thromb. Vasc. Biol.* **2007,** *27*, 1206-1212.

3.   Peter, K.; Bode, C., A deletion in the alpha subunit locks platelet integrin alpha IIb beta 3 into a high affinity state. *Blood coagulation & fibrinolysis : an international journal in haemostasis and thrombosis* **1996,** *7* (2), 233-6.

4.   Tromsdorf, U. I.; Bruns, O. T.; C, S. S.; Beisiegel, U.; Weller, H., A Highly Effective, Nontoxic T_1 MR Contrast Agent Based on Ultrasmall PEGylated Iron Oxide Nanoparticles. *Nano Lett* **2009,** *9*, 4434-4440.

5.   Kim, B. H.; Lee, N.; Kim, H.; An, K.; Park, Y. I.; Choi, Y.; Shin, K.; Lee, Y.; Kwon, S. G.; Na, H. B.; Park, J. G.; Ahn, T. Y.; Kim, Y. W.; Moon, W. K.; Choi, S. H.; Hyeon, T., Large-Scale Synthesis of Uniform and Extremely Small-Sized Iron Oxide Nanoparticles for High-Resolution T_1 Magnetic Resonance Imaging Contrast Agents. *J. Am. Chem. Soc.* **2011,** *133*, 12624-12631.

6.   Hu, F.; Jia, Q.; Li, Y.; Gao, M., Facile synthesis of ultrasmall PEGylated iron oxide nanoparticles for dual-contrast T_1- and T_2-weighted magnetic resonance imaging. *Nanotechnology* **2011,** *22*, 245604-245611.

7.   Pothayee, N.; Pothayee, N.; Jain, N.; Hu, N.; Balasubramaniam, S.; Johnson, L. M.; Davis, R. M.; Sriranganathan, N.; Riffle, J. S., Magnetic Block Ionomer Complexes for Potential Dual Imaging and Therapeutic Agents. *Chem. Mater.* **2012,** *24*, 2056-2063.

8.   Pothayee, N.; Balasubramaniam, S.; Pothayee, N.; Jain, N.; Hu, N.; Lin, Y.; Davis, R. M.; Sriranganathan, N.; Koretsky, A. P.; Riffle, J. S., Magnetic nanoclusters with hydrophilic spacing for dual drug delivery and sensitive magnetic resonance imaging. *J. Mater. Chem. B* **2013,** *1*, 1142-1149.

9.   Neuwelt, E. A.; Hamilton, B. E.; Varallyay, C. G.; Rooney, W. R.; Edelman, R. D.; Jacobs, P. M.; Watnick, S. G., Ultrasmall superparamagnetic iron oxides (USPIOs): a future alternative magnetic resonance (MR) contrast agent for patients at risk for nephrogenic systemic fibrosis (NSF)? *Kidney Int.* **2009,** *75*, 465–474.

10.   Wang, Y. X. J., Superparamagnetic iron oxide based MRI contrast agents: Current status of clinical application. *Quant Imaging Med Surg.* **2011,** *1*, 35-40